Title

Strong and ductile FeNiCoAl-based high-entropy alloys for cryogenic to elevated temperature multifunctional applications

Authors

Zhang, Cheng

Yu, Qin

Tang, Yuanbo T

et al.

Publication Date

2023

DOI

10.1016/j.actamat.2022.118449

Strong and Ductile FeNiCoAl-based High-Entropy Alloys for Cryogenic to Elevated Temperature Multifunctional Applications

Cheng Zhang[1,‡], Qin Yu[2,3,‡], Yuanbo T. Tang[4,‡], Mingjie Xu[1], Haoren Wang[5], Chaoyi Zhu[6], Jon Ell[2,3], Shiteng Zhao[3], Benjamin E. MacDonald[1], Penghui Cao[1], Julie M. Schoenung[1], Kenneth S. Vecchio[5]*, Roger C. Reed[4], Robert O. Ritchie[2,3]*, Enrique J. Lavernia[1]*

[1] Department of Materials Science and Engineering, University of California Irvine, Irvine, CA 92697-2585, USA

[2] Materials Sciences Division, Lawrence Berkeley National Laboratory, Berkeley, CA 94720, USA

[3] Department of Materials Science and Engineering, University of California, Berkeley, CA 94720, USA

[4] Department of Materials, University of Oxford, Parks Road, Oxford, OX1 3PH, United Kingdom

[5] Department of NanoEngineering, University of California San Diego, La Jolla, CA 92093-0448, USA

[6] Department of Materials Science and Engineering, Carnegie Mellon University, Pittsburgh, PA 15213, USA

[‡] These authors contributed equally. *Corresponding authors.

Emails: kvecchio@eng.ucsd.edu; roritchie@lbl.gov; lavernia@uci.edu.

Abstract: The highly tunable properties of multi-principal element alloys, commonly known as high-entropy alloys (HEAs), provide a remarkable potential for the development of superior materials for critical structural applications that involve extreme conditions. However, the optimization of the properties of HEAs has been primarily limited to behavior either low or high temperatures. Here, we report on a non-equiatomic, heterostructured, high-entropy alloy FeNiCoAlTaB which possesses remarkable combinations of mechanical properties across a wide range of temperatures from 77 K to 1073 K. The current metastable alloy presents good ductility and superior engineering tensile strengths of 2.2 GPa, 1.4 GPa, 800 MPa, and 500 MPa at 77 K, 298 K, 873 K, and 1073 K, respectively. This behavior is achieved by a synergic sequence of individual mechanisms that are activated at different temperatures. The alloy even displays pseudoelasticity at 77 K with an applied load up to 2 GPa. This work provides a methodology for tailoring structural heterogeneity and metastability in the design and fabrication of multifunctional HEAs that will outperform known metals and alloys over a wide range of temperatures.

Keywords: High-entropy alloy; strength-ductility synergy; pseudoelasticity; cryogenic temperatures; elevated temperatures; heterogeneous structures

1. Introduction

Our timeless curiosity about outer space has fueled truly astounding technological advances as evidenced by accomplishments ranging from Lunar exploration to Mars voyages. The temperature on the surfaces of planets in the solar system varies drastically from as high as 750 K (Venus) to as low as 70 K (Neptune). Accordingly, structural materials used for space exploration must bear suitable performance across a broad range of temperatures. Although conventional metals and alloys can be tuned to possess excellent mechanical properties, the improvement is often limited to specific temperature ranges [1][2]. The past decade has witnessed the emergence of the concept of complex concentrated alloys, commonly referred to as high-entropy alloys (HEAs), where multiple principal elements are co-solidified into single- or multi-phase systems [3][4][5][6]. The highly tunable properties of these alloys provide a fascinating potential for developing materials with unprecedented mechanical properties for critical applications under extreme conditions [7][8][9][10][11]. For example, face-centered-cubic (*fcc*) HEAs composed of transition metal elements have demonstrated exceptional strength-ductility synergy, and hence fracture toughness, at ambient-to-cryogenic temperatures [12][13][14][15][16]. Some body-centered-cubic (*bcc*) refractory HEAs, conversely, exhibit ultrahigh strength at elevated temperatures [17][18]. Nevertheless, the optimization of the properties of HEAs has been gained mostly in narrow ranges for either low- or high-temperature performance. As such, it is of particular interest to improve the mechanical properties of HEAs over a broad range of operating temperatures for their potential application in outer space exploration and other extreme environment applications.

A variety of salient strengthening mechanisms are active in conventional metallic and multiple principal element alloys; however, most mechanisms operate effectively only in certain temperature ranges. For instance, heterogeneous structures, realized by partial recrystallization,

rapid sintering, or mechanical surface treatments, have been established as an effective avenue to overcome the strength-ductility trade-off by suppressing early necking at ambient and cryogenic temperatures [19][20][21]. However, at elevated temperatures the stability of heterogeneous structures may be diminished due to grain growth, leading to a significant drop in strength with increase in temperature. Similarly, twinning-induced plasticity (TWIP) and transformation-induced plasticity (TRIP) are usually employed to improve the mechanical properties of alloys such as Fe-Mn-based and Fe-Cr-based stainless steels [22][23] at ambient and lower temperatures. However, the TWIP mechanism is far less effective at elevated temperatures due to reduced work hardening resulting from an increasing rate of dynamic recovery and the suppression of deformation twinning. As for TRIP steels, strengthening via martensitic transformation is curtailed once the temperature exceeds the martensite start (M_s) temperature near 600 K. To sustain a high strength at elevated temperatures, coherent precipitation strengthening is commonly employed as an effective mechanism, *e.g.* gamma prime (γ') hardening in Ni-base superalloys. This concept has been successfully implemented in some HEAs to achieve considerable strength at ambient temperatures [13][24][25][26]. However, limited work has been conducted to investigate the mechanical properties of precipitation-strengthened HEAs at elevated temperatures. In short, the effectiveness of individual strengthening mechanisms is often restricted to a specific (low or high) range of temperature. This leads to an intriguing quest: can we incorporate those beneficial mechanisms synergistically in an HEA to enable superior mechanical properties over a wide range of cryogenic to elevated temperatures?

To address this, we designed a non-equiatomic, heterostructured high-entropy alloy – FeNiCoAlTaB - which attains superb mechanical properties at temperatures from 77 K to 1073 K, by inducing various strengthening mechanisms which can be activated and operated effectively at

different temperatures. Specifically, this metastable alloy displays superior tensile strengths at 2.2 GPa, 1.4 GPa, 800 MPa, and 500 MPa at 77 K, 298 K, 873 K, and 1073 K, respectively, while maintaining tensile ductility over 12%. In addition, our HEA exhibits pseudoelasticity at 77 K, making this alloy a potential candidate for ultra-strong actuator or high-damping applications at cryogenic environments. This work provides a viable methodology for tailoring structural heterogeneity and metastability for designing and fabricating HEAs that outperform the mechanical properties of traditional metals and alloys over a wide range of temperatures.

2. Material and Methods

2.1 Materials Preparation

The raw ingots of the Fe-28.2Ni-17Co-11Al-2.5Ta-0.04B (at.%) HEA were produced by arc-melting raw high-purity metals (> 99.9 wt.%) in argon atmosphere. Each ingot was flipped and re-melted at least five times. To ensure a chemical homogeneity, samples were treated by induction heating at high power (at ~1573 K) for 1 hr, followed by turning and retreatment for a further 1 hr. After homogenization, samples were subsequently hot rolled at 1523 K with reduction in thickness by 20 to 30%, cold rolled with reduction in thickness by 90%, annealed at 1473 K for 10 min, and aged at 873 K for 2 hr. The severe cold rolling and annealing steps produce a heterogeneous structure with the NiAl B2-type precipitates along the grain boundaries. The NiAl particles, which remain stable at temperatures in excess of 1373 K, help improve the thermal stability of the heterostructure at high temperatures. In addition to the heterostructure and grain-boundary NiAl precipitates, the final 873 K aging resulted in the precipitation of nanoscale γ' particles. The volume fraction of NiAl after aging was $3.8 \pm 0.5\%$, mainly along grain boundaries.

2.2 Mechanical characterization

2.2.1 Monotonic tensile tests at temperatures from 77K to 1073K

Dogbone-shaped plate specimens were fabricated by electrical discharge machining and used to characterize the uniaxial tensile stress-strain curves at 77K, 298K, 873K, and 1073K. The FeNiCoAlTaB HEA samples having a gauge length of 20 mm and a cross-section of 3×0.5-0.7 mm^2 were used for the tensile tests at ambient temperature (298 K). Before testing, the sample surfaces were carefully ground and polished to a mirror surface with SiC papers up to 4000 grit. Ambient-temperature tensile testing was conducted on an Instron model 5982 load frame (Instron Corp., Norwood, MA, USA) under displacement control at a strain rate of 10^{-3}/s. Engineering strain within the gauge length was measured using an axial extensometer.

At cryogenic temperatures (77 K), FeNiCoAlTaB samples with a gauge dimensions of 17 × 1.5 × (0.5-0.7) mm^3 were used to characterize the tensile properties. Tensile tests were performed on an electro servo-hydraulic MTS 831 load frame (MTS Corp., Eden Prairie, MN, USA), equipped with a 10 kN load cell, at an engineering strain rate of 1.0×10^{-3} s^{-1}. During the test, the entire samples were submerged in a liquid-nitrogen bath. A low-temperature axial extensometer Model 3442 (Epsilon, USA) was employed to measure the engineering strain. Two tests were repeated for each condition.

High-temperature tensile properties were measured using an Instron Electro-Thermal Mechanical Testing (ETMT) system, equipped with a 5 kN load cell. Specimens were first electro discharge machined from plates into a dogbone shape with a total length of 40 mm and a gauge cross-sectional area of 2×0.5-0.7 mm^2. Recast layers induced by such machining were subsequently removed using abrasive media, finishing with 4000-grit paper. A K-type thermocouple was then spot welded at the center of the specimen to control the temperature during the test. The specimen was mounted between two water-cooled grips to establish a parabolic temperature distribution along the loading direction. This allows the central region of ~3 mm

within the gauge length to maintain a steady-state temperature; as this is where the deformation was localized, this was used as the effective gauge length. The strain measurement was conducted using a non-contacting digital image correlation video extensometer, where a speckle pattern is applied to the surface of the specimens with high-temperature paint for tracking purposes. The video data were recorded at 10 frames per second and analyzed using the iMetrum Video Gauge software [27]. The specimen was brought to temperature by direct resistance heating using a direct current (DC) through the specimen at a heating rate of 10 $K \cdot s^{-1}$ up to 1073 K. The sample was then isothermally held for 1 min. Tensile loading was carried out at a strain rate of ~10^{-3} s^{-1} until failure. As the DC-current heating immediately shuts off at the fracture point due to open circuit conditions, the microstructure was therefore preserved via rapid air quenching. Two tests were conducted at each condition.

2.2.2 Cyclic loading-unloading tensile tests at 77K

To probe the existence of pseudoelasticity in the FeNiCoAlTaB alloy at cryogenic temperatures, we carried out tensile loading-unloading tests at 77K using the same experimental setup and the same dogbone-shaped specimens as described above for the monotonic tensile test measurements. The strain during the first cycle was taken to 2% before unloading. The maximum strain in the subsequent cycles was increased by 1.5% for each cycle, with a total of seven loading-unloading cycles performed. The loading and unloading strain rates were controlled at 1.0×10^{-3} s^{-1}.

2.3 Materials characterization

The grain structure and grain orientation of the FeNiCoAlTaB alloy samples were characterized by a field-emission scanning electron microscopy (SEM) FEI Quanta3D (FEI Co., Hillsboro, Oregon, USA) equipped with an Oxford Instruments Electron Back-Scatter Diffraction

(EBSD) detector operated at 20 kV. The Oxford Aztec (Tango) software was employed to collect the EBSD data [28]. Related EBSD-based geometry necessary dislocation (GND) density maps and kernel average misorientation (KAM) maps were produced by our in-house program [28][29]. The EBSD-based GND density was derived from the crystal orientation data. Values of the dislocation density related to a particular type of dislocations can be calculated through constructing the Nye dislocation density tensor with the use of detected misorientation gradients. In the current work, the typical <110>{111} dislocation configurations in the *fcc* crystal structure were hypothesized as twelve edge and six screw dislocations. A Rigaku Smartlab X-ray diffractometer was used to detect phases in specimens before and after tensile testing.

The dislocation/twin substructures of the FeNiCoAlTaB alloy were characterized using a JEM-2800 transmission electron microscope (TEM) operated at 200 kV. Energy-dispersive x-ray spectroscopy (EDS) mapping was carried out in a STEM (JEOL, Grand Arm) operated at 300 kV. Kernel average misorientation (KAM) maps for deformed samples after tensile tests were acquired with the NanoMegas precession electron diffraction (PED) system that is installed in the JEM-2800 TEM. The step size was between 2 and 20 nm. TEM samples were prepared by focused Ga+ ion beam milling in the FIB-SEM (FEI Dual Beam focus ion beam SEM). The *in situ* TEM heating experiment was conducted in the JEM-2800 TEM with a cooling/heating holder (95 K -298 K).

2.4 Alloy Design

A Fe-(26-30)Ni-(12-20)Co (at.%) composition was first chosen as the matrix alloy due to its low martensite start (M_s) temperature and formation of plate-like martensite [30]. To strengthen the matrix, aluminum (Al) was chosen to form the nanoscale $L1_2$ precipitates, which can further decrease the M_s temperature [31][32]. Tantalum (Ta) was added to the FeCoNiAl matrix to provide solid-solution strengthening. Since Ta is a strong γ′ former in Ni-based superalloys and can

effectively increase the solvus temperature of γ′ [33], the addition of Ta makes the γ′ precipitates more stable at elevated temperatures in order to maintain high-temperature strength. To strengthen the grain boundaries, a small amount of boron (B) was added to decorate the boundaries [34]. This use of boron has also been employed to strengthen specific HEAs [35]. In addition, the formation of NiAl B2 particles improves the thermal stability of the heterogeneous structure at elevated temperature due to their grain boundary pinning effect [36].

The final composition Fe-28.2Ni-17Co-11Al-2.5Ta-0.04B (at.%) was optimized by the CALPHAD method by using Thermo-Calc CALPHAD software with the third version of the thermodynamic database developed specifically for HEAs (TCHEA). When compared with the Fe-27.5Ni-16.5Co-10Al-2.2Ta-0.04B (at.%) alloy [37], more Ni, Al, and Ta were added to strengthen the matrix and promote the precipitation of γ′ particles. The evolution of different phases with temperature is shown in Fig. S1 in the Supplementary Materials. The solvus temperature of $L1_2$ γ′ precipitates (including Ni_3Al and Ni_3Ti type) can reach nearly 1273 K, which would give rise to reasonable strength at elevated temperatures. As the solvus temperature of NiAl, B2 particles can never exceed 1473 K, this ensures that the thermal stability of the heterogeneous structure at elevated temperatures.

3. Results

3.1 Microstructure

We term our non-equiatomic high-entropy alloy FeNiCoAlTaB; its actual composition in at.% is Fe-28.2Ni-17Co-11Al-2.5Ta-0.04B. This alloy was designed to have high solvus temperatures of γ′ and B2 precipitates over 1173 K and 1373 K, respectively, which would ensure high strength and thermal stability at elevated temperatures, as shown in Fig. S1. After thermomechanical processing, a heterogeneous austenite structure was obtained comprising a

mixture of equiaxed fine grains and elongated coarse grains in the recrystallized state (Fig. 1a). The average sizes of the fine and coarse grains are 5.4 ± 3.8 μm and 28.4 ± 11.7 μm, respectively, which indicates a noticeable inhomogeneous distribution of grain sizes (Fig. S2). The grain boundaries of the heterostructure are decorated with NiAl B2-type particles, sized between ~0.5 and 2 μm (Fig. 1b). Our thermal stability characterization reveals that these intergranular NiAl precipitates persist at elevated temperatures up to 1400 K (Fig. 2). This suggests that the NiAl precipitates should be able to suppress grain-boundary migration and hence restrict the growth of fine grains *via* a Zener's pinning effect at elevated temperatures. Consequently, the heterostructure of the FeNiCoAlTaB alloy maintains good thermal stability up to 1400 K, a characteristic that is superior to most of other heterostructured metals and alloys [14][38]. In addition, the aging treatment generates the precipitation of coherent γ′ particles sized at 3 to 7 nm with a high volume fraction (28.2 ± 2.4%) in the *fcc* matrix (Fig. 1c). The γ′ precipitates were found to be enriched in Al, Ta, and Ni (Figs. 1d and S3) with a solvus temperature exceeding 1173 K (Fig. S4); this is akin to the γ′ precipitation reported for superalloys [33]. The diffraction patterns obtained from X-ray diffraction (XRD) show that the initial specimen has a single *fcc* phase (Fig. S5). The volume fraction of NiAl B2 particles is as small as 3.5%, which cannot be detected by XRD (usually the volume fraction of detectable phase has to exceed ~5%). The X-ray peaks of the γ′ precipitates are very close to those of *fcc*, which almost overlap.

3.2 Tensile properties over a wide temperature range

The uniaxial tensile properties of the FeNiCoAlTaB HEA were measured across a wide range of temperatures from 77 K to 1073 K. As shown in the engineering stress-strain curves in Fig. 3a, the tensile strength at room temperature reaches ~1.43 GPa corresponding to a tensile ductility of ~21%, representing an exceptional synergy of strength and ductility. When the temperature is

reduced to 77 K, the tensile strength increases to ~2.2 GPa without showing much compromise in ductility (which remains over 12%). In line with the high strength levels, considerable rates of strain hardening were observed exceeding ~15 GPa and ~4 GPa at 77 K and 298 K, respectively (Fig. 3b). At elevated temperatures, FeNiCoAlTaB maintains high levels of tensile strength at values exceeding 800 MPa and 500 MPa at 873 K and 1073 K, respectively. Accordingly, it is apparent that FeNiCoAlTaB exhibits exceptional strength properties over a wide range of temperatures from 77 K to 1073 K.

Figure 3c shows a comparison of the tensile strengths as a function of the deformation temperature (77-1073 K) of the FeNiCoAlTaB alloy with those of other high-performance metals and alloys, including nanocrystalline metals [1], refractory metals [39], steels [22][23], HEAs [40][41][42][43][44] and superalloys [23][33][45][46]. It can be seen that the FeNiCoAlTaB alloy has a higher tensile strength than these other metallic alloys by, respectively, 35% to 110% at 77 K and by 20% to 100% at 298 K. Moreover, at elevated temperatures in the range of 873 K and 1073 K, it maintains superior high-temperature strengths comparable to those of Inconel 625 and Haynes 25 superalloys. Significantly, the tensile strengths of the FeNiCoAlTaB HEA are, respectively, ~70% and 2.4 times higher than those of well-known equiatomic CrMnFeCoNi Cantor HEA at 873 K and 1083 K.

3.3 Pseudoelasticity at 77 K

As observed in Fig. 3b, the deformation of the FeNiCoAlTaB alloy at 77 K shows an abnormal resurgence in strain hardening, reaching a strain-hardening rate of ~18 GPa at a true strain of ~0.095; this is an order of magnitude higher than conventional metals and alloys. Such a rising strain-hardening rate is similar to that observed in shape-memory or pseudoelastic alloys [47], where a reversible martensitic transformation is active. To verify the existence of

pseudoelasticity at cryogenic temperatures in FeNiCoAlTaB, we performed incremental tensile loading-unloading tests at 77K. The resulting cyclic loading-unloading curves at 77K are shown in Fig. 4a.

The variation in the forward strain ($\varepsilon_{Forward}$), recoverable strain ($\varepsilon_{Recoverable}$), pseudoelastic strain ($\varepsilon_{Pseudoelastic}$), and strain recovery ratio ($\varepsilon_{Recoverable}/\varepsilon_{Forward}$) with respect to the loading cycles are presented in Fig. 4b. As schematically illustrated in Fig. 4a, the forward strain ($\varepsilon_{Forward}$) and recoverable strain ($\varepsilon_{Recoverable}$) in each loading cycle refer to the total proceeding strain and the total reversed strain developed during the loading and unloading phases, respectively. The pseudoelastic strain in a specific cycle was defined as the recoverable strain minus the elastic strain, which was calculated from the maximum stress, prior to unloading, divided by the Young's modulus; the latter property was measured from the first cycle of the tensile loading curve (Fig. 4a). As shown in Figs. 4a and b, the FeNiCoAlTaB alloy exhibits typical pseudoelastic behavior in that it displays a large nonlinear recoverable strain upon unloading. The strain recovery ratio ($\varepsilon_{Recoverable}/\varepsilon_{Forward}$) attains 85% in the 1st cycle and slightly decreases in the subsequent cycles to ~75% by the 7th cycle. The pseudoelastic strain shows a fast increase to a steady level at ~1.8% in the 3rd cycle, accompanied by a resurgence in strain hardening. The coupling of pseudoelasticity with increasing work-hardening capability suggests the operation of a reversible martensite transformation, which was confirmed by transmission electron microscopy (TEM), as described below. It should be noted here that the large strain recovery ratio (~84%), in particular at the small applied strain (~2-3%), cannot be attributed to the conventional Bauschinger effect that is commonly observed in the heterostructured metals and alloys. Although strain recovery during unloading can also be produced by Bauschinger effect, the driving force for such strain recovery is the buildup of long-range back stresses induced by the storage of geometrically-

necessary dislocations (GNDs) during the forward loading. Such back-stresses resist forward dislocation motion and assist reverse glide. However, the strain recovery ratio resulting from Bauschinger effect is usually small, *e.g.*, only ~30% [38][48][49] for Ti and FeNiCoAl-based HEA with heterogeneous lamella (HL) structures, which is much smaller than that caused by reverse martensitic transformation in typical superelastic alloys (> 80% in the first two cycles in our HEA).

Due to the existence of pseudoelasticity, the unloading and reloading curves form a hysteresis stress-strain loop with detectable width (Fig. 4a). The hysteresis effect indicates that mechanical energy can be dissipated in the FeNiCoAlTaB HEA during cyclic loading and unloading. Specifically, the variations in the characteristic energies under the loading-unloading curves ($E_{Consumed}$, $E_{Dissipated}$, $E_{Elastic}$ as illustrated in Fig. 4a) can be quantified for each cycle. As shown in Fig. 4c, the energy dissipated by pseudoelastic (or viscoelastic) deformation ($E_{Dissipated}$) increases quickly and remains at a steady level starting from the 3rd cycle. The energy dissipation ratio of the FeNiCoAlTaB alloy exceeds ~9% when the stress levels are ~1.2 GPa, which implies a good damping capacity of this HEA in a cryogenic environment.

Indeed, other HEAs, *e.g.*, the strongly textured Fe-28Ni-17Co-11.5Al-2.5Ta-0.05B (at.%) alloy (cold rolled to a reduction in thickness of 98.5% and annealed at 1573 K for 18 h to achieve bamboo-like structure) has been shown to exhibit significant superelasticity at room temperature [50]. However, this alloy requires complex processing, even in the single-crystal state [50][51][52], and involves a *fcc-bct-bcc* transformation which has yet to be verified [50][53]. Moreover, the tensile ductility of this alloy is only ~5% at room temperature [51][54], and it only displays superelasticity in the textured condition. By comparison, the current FeNiCoAlTaB HEA, where the processing is far more simplified, exhibits reasonable superelasticity under cryogenic conditions with random grain orientations.

It is pertinent to note here that this pseudoelastic behavior is prevalent in the FeNiCoAlTaB HEA at 77 K at high stress levels that exceed ~1.2 GPa and reach as high as ~2.1 GPa. Such ultrahigh stress levels cannot be achieved in conventional NiTi, Cu-based, and Fe-based alloys that display pseudoelasticity. For high-performance cryogenic HEAs, such as the CrMnFeCoNi and CrCoNi, the pseudoelasticity phenomenon is absent due to the lack of a *reversible* martensitic transformation [12][55][56]. In light of this, we believe that the FeNiCoAlTaB HEA is the strongest bulk polycrystalline alloy reported to date which additionally shows pseudoelastic behavior at cryogenic temperatures. This implies that this alloy is an excellent candidate for use as a high-strength smart material for high-damping or actuator applications in cryogenic environments, *e.g.*, for outer space exploration.

4. **Discussion**

4.1 Deformation mechanisms at 77 K

To discern the deformation mechanisms underlying the ultrahigh strain hardening and pseudoelasticity at 77 K, microstructures were characterized *postmortem* in tensile samples unloaded from strain levels of ~2%, ~4%, ~7%, and ~12%. The EBSD band contrast maps in Fig. S6 show that residual martensite mainly lies in the fine-grained regions when the applied strains reach 2% and 4%. A small amount of residual martensite is found on unloading when the strain is ~2%, indicating that martensitic transformation occurs in the first forward loading to ~2% at 77 K. The typical hysteresis loops and large strain recovery ratio (>80%) in the first two cycles further confirm that martensitic transformation is occurring (Fig. 4a). Figure S7 shows the relationship between the volume fraction of the residual martensite and the applied strain. It is found that the amount of stress-induced martensite increases with increasing strain, which is consistent with the development of increased strain hardening (Fig. 3b). When the strain reaches 10%, the stress-

induced martensitic transformation saturates, giving rise to the maximum strain-hardening rate. Beyond the peak of the hardening rate where martensitic transformation is no longer active, the generation of dislocations cannot sustain such a high rate of strain hardening (no deformation twins or microbands are found at 77 K after testing), which leads to the drop in the strain-hardening rate. Based on the data from the XRD results (Fig. S5), the lattice parameter of the *fcc* matrix is a_0 = 0.3605 nm, whereas the lattice parameter of the *bcc* martensite is a = 0.2908 nm. We can use the Bain model to calculate the maximum superelastic strains along <001>, <011> and <111> orientations based on lattice deformation theory [47][57]. The evaluated maximum superelastic strain along <001>, <011> and <111> is 14.1%, 1.4%, and 4.2%, respectively. Once the internal strain exceeds the maximum superelastic strains along the various crystal orientations, the stress-induced martensite cannot completely recover to the original austenite. Therefore, in the FeNiCoAlTaB HEA, residual martensite is more likely to appear in fine grains with orientations that achieve small superelasic strains.

Figure 5a shows the microstructure in the sample unloaded from a tensile strain of ~7%. Residual martensitic regions can be observed located mostly in the fine grains (blue arrows in Fig. 5a). This confirms the occurrence of martensitic transformation and further implies that the transformation is driven by the concentrated stress localized at the fine grains which can be ascribed to inhomogeneous deformation within the heterogeneous microstructure. Such deformation behavior is different from that in the strong-textured specimen (Fe-27.5Ni-16.5Co-10Al-2.2Ta-0.04B alloy) with bamboo-like structure, where the tensile ductility at 77 K is limited to less than 2% [37]. When the strain increases to ~12%, pronounced regions of martensite are detected which are almost fully extended throughout the fine grains (blue arrows in Fig. 5b) and further spread into the coarse grains (red arrows in Fig. 5b). The sequential martensitic

transformation strategy in this heterostructured HEA successfully overcomes early failure along grain boundaries during the martensitic transformation, which can help to extend the ductility in superelastic alloys with thin-plate martensite. In other words, martensitic transformation first takes place in the fine grains due to more martensite nucleation sites. The coarse grains play a role in suppressing the crack extension from the fine grains, which is similar to that in the recent eutectic herringbone high-entropy alloys [58]. The fracture occurs when the strain-hardening rate is still very high. This premature failure is ascribed to the severe stress concentration located at the stress-induced martensite interfaces and/or the triple joints [59]. TEM imaging reveals that two variants of martensite are formed in both the coarse and fine grain regions, as shown by the embedded TEM diffraction patterns and precession electron diffraction maps in Figs. 5c and e. The thickness of the martensite variants was found to be ~50 nm in the coarse grain regions (Fig. 5c) and ~200 nm in the fine grains (Fig. 5e). High-resolution TEM imaging further revealed the formation of high-density nanotwins with an ultrafine spacing of 6-10 nm with very few stacking faults along the twin boundaries inside the stress-induced martensite, as is evident in Figs. 5d and f. This suggests that the combined hardening effects of hetero-deformation induced martensite transformation along with the nanotwinning inside the martensite regions are responsible for the extraordinary strain-hardening capability of the FeNiCoAlTaB HEA during deformation at 77 K.

From Figs. 5c and e, it is apparent that the residual martensite in our alloy possesses a thin-plate morphology. Among various types of martensite observed in Fe-Ni-based alloys, only thin-plate martensite is known to display reversible transformation [47]. Therefore, the pseudoelastic strain observed upon unloading at 77 K can almost certainly be ascribed to the reverse transformation of the thin-plate martensite. However, as seen in Fig. 4, when the applied strain level exceeded ~4%, the residual strain increased whereas the pseudoelastic strain reached a steady

value, indicating that at this stage the regions of the thin-plate martensite are unable to be fully reversed under large deformation. This irreversibility in the martensitic transformation is likely caused by the development of dislocation structures and nanotwins within the martensitic structure that block the reverse transformation. Such marked dislocation activity within the martensitic regions can be visualized in the kernel average misorientation (KAM) maps (Fig. 6) taken from the martensite regions characterized in Figs. 5c and e, where local misorientation in the KAM map can be used to show the dislocation activity. It should be noted here that no phase transformation of the residual martensite occurs during the heating from the test temperature, 77 K, to room temperature, as evidenced by the *in situ* TEM heating characterization shown in Fig. 7.

4.2 Deformation mechanisms at 298 K

Apart from the superior cryogenic properties, the ambient temperature strength of the FeNiCoAlTaB HEA is also very high with a value as high as 1.4 GPa with a tensile ductility over 20% (Fig. 3a). The extraordinary strain-hardening capability of the alloy can be primarily attributed to hetero-deformation induced hardening [60], which originates from the development of geometrically-necessary dislocations (GNDs) that act to suppress localized plastic instabilities and thereby enhance the ductility at a high strength level [19]. The incompatible deformation between coarse and fine neighboring grains leads to the generation of heterogeneously distributed GNDs with a higher density in the fine grain regions and a lower density in the coarse grain domains (Figs. 8a and b). The stable heterostructure during the entire process of plastic deformation sustains this generation of GNDS which continuously maintains a high strain-hardening rate of ~4-5 GPa (Fig. 3b). Apart from the hetero-deformation induced hardening, strengthening from the martensitic transformation does not occur at 298 K – we presume due to insufficiently high stress levels at this temperature. However, deformation-induced microbands

are observed (Fig. 8c). The formation of the microbands plays a role in grain refinement and triggers so-called microband-induced plasticity strengthening *via* a dynamic Hall-Petch effect [61][62]. Similar to what has been found in an aged $(FeNiCo)_{86}Al_7Ti_7$ HEA [13], this unique strengthening effect in FeNiCoAlTaB enables outstanding plastic stability at high strength levels to delay premature failure. It is noticeable that deformation failure occurs immediately without any indication of necking. This may be correlated to the local stress concentration caused by NiAl particles along grain boundaries. The current authors previously systematically investigated the precipitation of NiAl along grain boundaries in the FeNiCoAlTaB HEA and found that NiAl precipitates along interfaces could cause severe stress concentration and premature failure [54].

At room temperature, the yield strength of the FeNiCoAlTaB HEA increases from 480 MPa (as shown in Fig. S8) to 890 MPa after aging. The increase in strength caused by the coherent nanoscale γ′ precipitates can be estimated from the following relationship [63]:

$$\Delta\sigma_p = 0.81M(\gamma_{APB}/2b)(3\pi f/8)^{1/2} \quad , \qquad (1)$$

where M is the Taylor factor (3.06 for polycrystalline *fcc* alloys), f is the volume fraction (0.28) of precipitates, b is the magnitude of the Burgers vector of the matrix (~0.27 nm), and γ_{APB} is the anti-phase boundary energy of the precipitated particles (γ_{APB} = 0.16 J/m^2, for Ni_3Al precipitates in Ni-based superalloys [64]). By substituting the above parameters into Eq. (1), the increase in stress is $\Delta\sigma_p$ ~ 420 MPa, which contributes significantly to the enhancement in yield strength. The calculation result is in good agreement with the experiment result.

4.3 Deformation mechanisms at 873 K and 1073 K

As noted above, the deformation behavior of the FeNiCoAlTaB HEA is also impressive at elevated temperatures up to 1073 K in that the alloy still maintains a synergy of high strength and ductility (Fig. 3). In contrast to many high-temperature refractory HEAs that suffer from rapid

grain growth with heating [65], the heterogeneous structure composed of fine-grained and coarse-grained domains in FeNiCoAlTaB does not degrade at high temperatures because of the grain-boundary pinning effect that arises from the thermodynamically stable grain-boundary NiAl phase (Fig. 2). In addition, the NiAl particles also provide grain-boundary cohesion to prevent intergranular failures or grain-boundary sliding that are often active as creep damage mechanisms at high temperatures. Indeed, the fracture surfaces shown in Fig. 9 reveal no evidence of intergranular failure. It is worth noting that the Achilles' heel of many high temperature materials, such as nickel-base superalloys, is the evolution of damage along the grain boundaries, in the form of boundary migration, brittle intergranular failure or more often cavitation; this can result in a ductility loss, particularly between 873-1073 K, where high-performance superalloys can fail at 2-3% engineering strain [66]. The tensile ductility of the FeNiCoAlTaB HEA, of 24% at 873 K and 22% at 1073 K, does demonstrate the potentially wider application of this alloy in this critical temperature regime.

The size of the γ′ precipitates (<10 nm) in the current HEA are much smaller than that in conventional Ni-based superalloys (>50 nm), which may lead to different interaction mechanisms between the precipitates and dislocations. Mechanistically, the FeNiCoAlTaB HEA shows notable work hardening and the Portevin-Le Chatelier effect with serrated plastic flow at 873 K. The plastic instability is likely to originate from insufficient recovery of dislocations at 873 K which causes repeated pinning of mobile dislocations at the nanoscale gamma prime (γ′) precipitates followed by subsequent dislocation bursts. This can be seen in Fig. 8f, where there is clear evidence that the dislocations are pinned by the γ′ particles. The spacing of dislocation pairs is over 30 nm, which is much larger than the size of the γ′ precipitates. In addition, extensive dislocations are observed to form on the primary {111} slip planes, where a high density of dislocations appear (Fig. S9a),

suggesting that dislocations shear the small γ′ precipitates [67]. In some areas, the dislocations were present as extended stacking fault ribbons (Fig. S9b), indicating that the deformation is localized [64][68]. The strengthening through the interaction of the dislocations with the precipitates provides the basis for the high strain-hardening rate as well as the favorable strength at 873K.

With the increase in temperature to 1073 K, the deformation mode changes in that dynamic dislocation pinning and work-hardening effects are diminished, the latter being evident by the marked reduction in the density of geometrically-necessary dislocations (Fig. 8h). This suggests that the temperature at 1073 K is sufficiently high to allow for dislocation recovery and bypassing of precipitates (Fig. 10a). Few dislocation loops are found in some local areas, indicating that the strengthening effect is caused by the precipitates with limited dislocation slip. Additionally, stacking faults are frequently observed (Fig. 8i), which provides a further active strengthening mechanism for impeding dislocation motion and retarding recovery mechanisms such as cross-slip [69]. The formation of the arrays of planar stacking faults in Fig. 10b could provide reasonable strengthening at 1073 K. Numerous studies have shown that high strengths at ambient to lower temperatures are attainable in *fcc* HEAs from their low stacking-fault energies [6][70], although few studies have focused on this effect at high temperatures. Specifically, the active strengthening mechanisms at elevated temperatures primarily involved ordered $L1_2$ gamma prime precipitates, with additional strengthening contributed by the stacking faults. As one of the planar faults observed in the *fcc* system, stacking faults can lead to hardening by affecting the mobility of dislocations or faults, and creating an energy penalty for thermally-activated cross-slip. In other alloys with the same crystallography and a higher fraction of precipitates, stacking faults also lead to anomalous yielding behavior while interacting with anti-phase boundaries and $L1_2$ precipitates.

For a low stacking-fault energy materials, *i.e.* with larger separations between the dissociated partials, it becomes harder to cross-slip as the partials need to first recombine into a segment of perfect dislocation on the glide plane and then separate on the cross-slip plane. Our results for the deformation of FeNiCoAlTaB in the range of 873 K to 1073 K strongly imply that the development of planar faults can also be crucial for attaining high strength.

5. Conclusions

A multifunctional, non-equiatomic, FeNiCoAlTaB high-entropy alloy has been designed to exhibit exceptional mechanical properties not uniquely at low or high temperatures but rather across a wide range of operating temperatures from 77 K to 1073 K. At cryogenic temperatures, plastic deformation was seen to involve a stress-induced martensitic transformation coupled with nanotwinning, the latter operating within the martensite phase, which provided a marked contribution to the alloy's ultrahigh strain-hardening rate and outstanding tensile strength. Due to the formation of thin-plate martensite, pseudoelasticity can also be achieved in this HEA at 77 K. The sequential martensitic transformation strategy in this heterostructured HEA successfully overcomes the early failure along grain boundaries during the martensitic transformation at 77 K. At ambient temperatures, hetero-deformation induced hardening and deformation-mediated microbands are responsible for the high strain-hardening rate and exceptional tensile strength and ductility properties. At 873 K, γ' precipitation strengthening acts as the primary factor for the alloy's high strength. With the coarsening of the precipitates and increased dislocation recovery at 1073 K, strengthening by dislocation dissociation and the consequent formation of stacking faults provides the dominant contributor to the high strength. The design of the microstructure of this FeNiCoAlTaB alloy, specifically to create a sequence of deformation and strengthening mechanisms active at different temperature ranges, provides a viable strategy for the development

of multifunctional HEAs with outstanding mechanical properties over an unprecedented range of operating temperatures - from cryogenic to elevated temperatures.

Acknowledgments:

We would like to thank Dr. Xin Wang, Calvin Harris Belcher, Fan Ye (UC Irvine), Dr. Li Xing (IMRI, UC Irvine), and Dr. Mingde Qin (UC San Diego) for assistance with some of the experiments. **Funding**: C.Z., B.E.M., and E.J.L. acknowledge support from the BIAM-UCI Research Center for the Fundamental Study of Novel Structural Materials (Research Agreement #210263). C.Z. and M.X. acknowledge the use of facilities and instrumentation at the UC Irvine Materials Research Institute (IMRI), which is supported in part by the National Science Foundation through the UC Irvine Materials Research Science and Engineering Center (DMR-2011967). J.M.S acknowledges support from the UCI Samueli School of Engineering and the Army Research Office (W911NF 18-1-0279). Q.Y. and R.O.R. acknowledge support from the U.S. Department of Energy, Office of Science, Office of Basic Energy Sciences, Materials Sciences and Engineering Division, under contract no. DE-AC02-05-CH11231.

References

[1] Y.M. Wang, E. Ma, R.Z. Valiev, Y.T. Zhu, Tough nanostructured metals at cryogenic temperatures, Adv. Mater. 16 (2004) 328–331.

[2] K. Lu, Stabilizing nanostructures in metals using grain and twin boundary architectures, Nat. Rev. Mater. 1 (2016) 16019.

[3] D.B. Miracle, O.N. Senkov, A critical review of high entropy alloys and related concepts, Acta Mater. 122 (2017) 448–511.

[4] B. Cantor, I.T.H. Chang, P. Knight, A.J.B. Vincent, Microstructural development in equiatomic multicomponent alloys, Mater. Sci. Eng. A. 375 (2004) 213–218.

[5] J. Yeh, S. Chen, S. Lin, J. Gan, T. Chin, T. Shun, C. Tsau, S. Chang, Nanostructured high-entropy alloys with multiple principal elements: novel alloy design concepts and outcomes, Adv. Eng. Mater. 6 (2004) 299–303.

[6] E.P. George, D. Raabe, R.O. Ritchie, High-entropy alloys, Nat. Rev. Mater. 4 (2019) 515-534.

[7] Z. Li, S. Zhao, S.M. Alotaibi, Y. Liu, B. Wang, M.A. Meyers, Adiabatic shear localization in the CrMnFeCoNi high-entropy alloy, Acta Mater. 151 (2018) 424–431.

[8] O.N. Senkov, G.B. Wilks, D.B. Miracle, C.P. Chuang, P.K. Liaw, Refractory high-entropy alloys, Intermetallics. 18 (2010) 1758–1765.

[9] O.N. Senkov, D.B. Miracle, K.J. Chaput, J.-P. Couzinie, Development and exploration of refractory high entropy alloys—A review, J. Mater. Res. 33 (2018) 3092–3128.

[10] Y. Zou, H. Ma, R. Spolenak, Ultrastrong ductile and stable high-entropy alloys at small scales, Nat. Commun. 6 (2015) 1–8.

[11] Q. Ding, Y. Zhang, X. Chen, X. Fu, D. Chen, S. Chen, L. Gu, F. Wei, H. Bei, Y. Gao, Tuning element distribution, structure and properties by composition in high-entropy alloys, Nature. 574 (2019) 223–227.

[12] B. Gludovatz, A. Hohenwarter, D. Catoor, E.H. Chang, E.P. George, R.O. Ritchie, A fracture-resistant high-entropy alloy for cryogenic applications, Science (80-.). 345 (2014) 1153–1158.

[13] T. Yang, Y.L. Zhao, Y. Tong, Z.B. Jiao, J. Wei, J.X. Cai, X.D. Han, D. Chen, A. Hu, J.J. Kai, Multicomponent intermetallic nanoparticles and superb mechanical behaviors of complex alloys, Science (80-.). 362 (2018) 933–937.

[14] Y.H. Jo, S. Jung, W.M. Choi, S.S. Sohn, H.S. Kim, B.J. Lee, N.J. Kim, S. Lee, Cryogenic strength improvement by utilizing room-temperature deformation twinning in a partially recrystallized VCrMnFeCoNi high-entropy alloy, Nat. Commun. 8 (2017) 1–8.

[15] L. Fan, T. Yang, Y. Zhao, J. Luan, G. Zhou, H. Wang, Z. Jiao, C.-T. Liu, Ultrahigh

strength and ductility in newly developed materials with coherent nanolamellar architectures, Nat. Commun. 11 (2020) 1–8.

[16] Y. Tong, D. Chen, B. Han, J. Wang, R. Feng, T. Yang, C. Zhao, Y.L. Zhao, W. Guo, Y. Shimizu, Outstanding tensile properties of a precipitation-strengthened FeCoNiCrTi0. 2 high-entropy alloy at room and cryogenic temperatures, Acta Mater. 165 (2019) 228–240.

[17] O.N. Senkov, S. Gorsse, D.B. Miracle, High temperature strength of refractory complex concentrated alloys, Acta Mater.175 (2019) 395-405.

[18] C. Lee, G. Kim, Y. Chou, B.L. Musicó, M.C. Gao, K. An, G. Song, Y.-C. Chou, V. Keppens, W. Chen, Temperature dependence of elastic and plastic deformation behavior of a refractory high-entropy alloy, Sci. Adv. 6 (2020) eaaz4748.

[19] Y. Zhu, K. Ameyama, P.M. Anderson, I.J. Beyerlein, H. Gao, H.S. Kim, E. Lavernia, S. Mathaudhu, H. Mughrabi, R.O. Ritchie, Heterostructured materials: superior properties from hetero-zone interaction, Mater. Res. Lett. 9 (2021) 1–31.

[20] E. Ma, X. Wu, Tailoring heterogeneities in high-entropy alloys to promote strength–ductility synergy, Nat. Commun. 10 (2019) 1–10.

[21] Z. Cheng, H. Zhou, Q. Lu, H. Gao, L. Lu, Extra strengthening and work hardening in gradient nanotwinned metals, Science 362 (2018) eaau1925.

[22] J.R. Davis, Stainless Steels, ASM International, 1994.

[23] R.M. McClintock, Mechanical Properties of Structural Materials at Low Temperatures, National Bureau of Standards, 1960.

[24] J.Y. He, H. Wang, H.L. Huang, X.D. Xu, M.W. Chen, Y. Wu, X.J. Liu, T.G. Nieh, K. An, Z.P. Lu, A precipitation-hardened high-entropy alloy with outstanding tensile properties, Acta Mater. 102 (2016) 187–196.

[25] F. He, D. Chen, B. Han, Q. Wu, Z. Wang, S. Wei, D. Wei, J. Wang, C.T. Liu, J. Kai, Design of D022 superlattice with superior strengthening effect in high entropy alloys, Acta Mater. 167 (2019) 275–286.

[26] Z. Fu, L. Jiang, J.L. Wardini, B.E. MacDonald, H. Wen, W. Xiong, D. Zhang, Y. Zhou, T.J. Rupert, W. Chen, A high-entropy alloy with hierarchical nanoprecipitates and ultrahigh strength, Sci. Adv. 4 (2018) eaat8712.

[27] S. Sulzer, E. Alabort, A. Németh, B. Roebuck, R. Reed, On the rapid assessment of mechanical behavior of a prototype nickel-based superalloy using small-scale testing, Metall. Mater. Trans. A. 49 (2018) 4214–4235.

[28] C. Zhu, T. Harrington, G.T. Gray, K.S. Vecchio, Dislocation-type evolution in quasi-statically compressed polycrystalline nickel, Acta Mater. (2018).

[29] C. Zhu, T. Harrington, V. Livescu, G.T. Gray, K.S. Vecchio, Determination of geometrically necessary dislocations in large shear strain localization in aluminum, Acta Mater. 118 (2016) 383–394.

[30] A. Shibata, H. Yonezawa, K. Yabuuchi, S. Morito, T. Furuhara, T. Maki, Relation between martensite morphology and volume change accompanying fcc to bcc martensitic transformation in Fe–Ni–Co alloys, Mater. Sci. Eng. A. 438 (2006) 241–245.

[31] H. Ohtsuka, S. Kajiwara, Effects of carbon content and ausaging on $\gamma \leftrightarrow \alpha'$ transformation behavior and reverse-transformed structure in Fe-Ni-Co-Al-C alloys, Metall. Mater. Trans. A. 25 (1994) 63–71.

[32] E. Hornbogen, W. Meyer, Martensitic transformatin of solid solution with coherent elements, Acta Metall. 15 (1967) 584–586.

[33] R.C. Reed, The Superalloys: Fundamentals and Applications, Cambridge University

Press, 2008.

[34] C.T. Liu, C.L. White, J.A. Horton, Effect of boron on grain-boundaries in Ni3Al, Acta Metall. 33 (1985) 213–229.

[35] J.B. Seol, J.W. Bae, Z. Li, J.C. Han, J.G. Kim, D. Raabe, H.S. Kim, Boron doped ultrastrong and ductile high-entropy alloys, Acta Mater. 141 (2018) 366-376.

[36] C.C. Jia, K. Ishida, T. Nishizawa, Partition of alloying elements between γ (A1), γ′(L1 2), and β (B2) phases in Ni-Al base systems, Metall. Mater. Trans. A. 25 (1994) 473–485.

[37] C. Zhang, C. Zhu, T. Harrington, L. Casalena, H. Wang, S. Shin, K.S. Vecchio, Multifunctional non-equiatomic high entropy alloys with superelastic, high damping, and excellent cryogenic properties, Adv. Eng. Mater. 1800941 (2018) 1–9.

[38] X. Wu, M. Yang, F. Yuan, G. Wu, Y. Wei, X. Huang, Y. Zhu, Heterogeneous lamella structure unites ultrafine-grain strength with coarse-grain ductility, Proc. Natl. Acad. Sci. 112 (2015) 14501–14505.

[39] N.E. Prasad, R.J.H. Wanhill, Aerospace Materials and Material Technologies, Springer, 2017.

[40] F. Otto, A. Dlouhý, C. Somsen, H. Bei, G. Eggeler, E.P. George, The influences of temperature and microstructure on the tensile properties of a CoCrFeMnNi high-entropy alloy, Acta Mater. 61 (2013) 5743–5755.

[41] Y. Lu, X. Gao, L. Jiang, Z. Chen, T. Wang, J. Jie, H. Kang, Y. Zhang, S. Guo, H. Ruan, Directly cast bulk eutectic and near-eutectic high entropy alloys with balanced strength and ductility in a wide temperature range, Acta Mater. 124 (2017) 143–150.

[42] Y. Lu, Y. Dong, S. Guo, L. Jiang, H. Kang, T. Wang, B. Wen, Z. Wang, J. Jie, Z. Cao, A promising new class of high-temperature alloys: Eutectic high-entropy alloys, Sci. Rep. 4

(2014) 1–5.

[43] T. Yang, Z. Tang, X. Xie, R. Carroll, G. Wang, Y. Wang, K.A. Dahmen, P.K. Liaw, Y. Zhang, Deformation mechanisms of $Al_{0.1}$CoCrFeNi at elevated temperatures, Mater. Sci. Eng. A. 684 (2017) 552–558.

[44] D. Li, Y. Zhang, The ultrahigh charpy impact toughness of forged AlxCoCrFeNi high entropy alloys at room and cryogenic temperatures, Intermetallics. 70 (2016) 24–28.

[45] E.F. Bradley, Superalloys: A Technical Guide, (1988).

[46] F.C. Campbell, Elements of Metallurgy and Engineering Alloys, ASM International, 2008.

[47] K. Otsuka, C.M. Wayman, Shape Memory Materials, Cambridge University Press, 1999.

[48] C. Zhang, C. Zhu, T. Harrington, K. Vecchio, Design of non-equiatomic high entropy alloys with heterogeneous lamella structure towards strength-ductility synergy, Scr. Mater. 154 (2018) 78–82. https://doi.org/10.1016/j.scriptamat.2018.05.020.

[49] C. Zhang, C. Zhu, K. Vecchio, Non-equiatomic FeNiCoAl-based high entropy alloys with multiscale heterogeneous lamella structure for strength and ductility, Mater. Sci. Eng. A. 743 (2019) 361–371. https://doi.org/10.1016/j.msea.2018.11.073.

[50] Y. Tanaka, Y. Himuro, R. Kainuma, Y. Sutou, T. Omori, K. Ishida, Ferrous polycrystalline shape-memory alloy showing huge superelasticity, Science (80-.). 327 (2010) 1488–1490.

[51] H. Fu, W. Li, S. Song, Y. Jiang, J. Xie, Effects of grain orientation and precipitates on the superelasticity in directionally solidified FeNiCoAlTaB shape memory alloy, J. Alloys Compd. 684 (2016) 556–563.

[52] J. Ma, B. Kockar, A. Evirgen, I. Karaman, Z.P. Luo, Y.I. Chumlyakov, Shape memory

behavior and tension–compression asymmetry of a FeNiCoAlTa single-crystalline shape memory alloy, Acta Mater. 60 (2012) 2186–2195.

[53] J. Ma, B.C. Hornbuckle, I. Karaman, G.B. Thompson, Z.P. Luo, Y.I. Chumlyakov, The effect of nanoprecipitates on the superelastic properties of FeNiCoAlTa shape memory alloy single crystals, Acta Mater. 61 (2013) 3445–3455.

[54] C. Zhang, C. Zhu, S. Shin, L. Casalena, K. Vecchio, Materials Science & Engineering A Grain boundary precipitation of tantalum and NiAl in superelastic FeNiCoAlTaB alloy, Mater. Sci. Eng. A. 743 (2019) 372–381. https://doi.org/10.1016/j.msea.2018.11.077.

[55] B. Gludovatz, A. Hohenwarter, K.V.S. Thurston, H. Bei, Z. Wu, E.P. George, R.O. Ritchie, Exceptional damage-tolerance of a medium-entropy alloy CrCoNi at cryogenic temperatures, Nat. Commun. 7 (2016) 1–8.

[56] M. Naeem, H. He, F. Zhang, H. Huang, S. Harjo, T. Kawasaki, B. Wang, S. Lan, Z. Wu, F. Wang, Cooperative deformation in high-entropy alloys at ultralow temperatures, Sci. Adv. 6 (2020) eaax4002.

[57] C. Zhang, X. Wang, M. Xu, B.E. MacDonald, R. Hong, C. Zhu, X. Dai, K.S. Vecchio, D. Apelian, H. Hahn, Orientation-dependent superelasticity of a metastable high-entropy alloy, Appl. Phys. Lett. 119 (2021) 161908.

[58] P. Shi, R. Li, Y. Li, Y. Wen, Y. Zhong, W. Ren, Z. Shen, T. Zheng, J. Peng, X. Liang, Hierarchical crack buffering triples ductility in eutectic herringbone high-entropy alloys, Science (80-.). 373 (2021) 912–918.

[59] S.M. Ueland, C.A. Schuh, Grain boundary and triple junction constraints during martensitic transformation in shape memory alloys, J. Appl. Phys. 114 (2013) 53503.

[60] Y. Zhu, X. Wu, Perspective on hetero-deformation induced (HDI) hardening and back

stress, Mater. Res. Lett. 7 (2019) 393–398.

[61] J.D. Yoo, K.-T. Park, Microband-induced plasticity in a high Mn–Al–C light steel, Mater. Sci. Eng. A. 496 (2008) 417–424.

[62] D.A. Hughes, Microstructural evolution in a non-cell forming metal: Al Mg, Acta Metall. Mater. 41 (1993) 1421–1430.

[63] A.J. Ardell, Precipitation hardening, Metall. Trans. A. 16 (1985) 2131–2165.

[64] R.C. Reed, C.M.F. Rae, Physical metallurgy of the nickel-based superalloys, in: Phys. Metall., Elsevier, 2014: pp. 2215–2290.

[65] O.N. Senkov, S.L. Semiatin, Microstructure and properties of a refractory high-entropy alloy after cold working, J. Alloys Compd. 649 (2015) 1110–1123.

[66] A.A.N. Németh, D.J. Crudden, D.E.J. Armstrong, D.M. Collins, K. Li, A.J. Wilkinson, C.R.M. Grovenor, R.C. Reed, Environmentally-assisted grain boundary attack as a mechanism of embrittlement in a nickel-based superalloy, Acta Mater. 126 (2017) 361–371.

[67] H. Gleiter, E. Hornbogen, Precipitation hardening by coherent particles, Mater. Sci. Eng. 2 (1968) 285–302.

[68] P.S. Kotval, The microstructure of superalloys, Metallography. 1 (1969) 251–285.

[69] X.G. Wang, J.L. Liu, T. Jin, X.F. Sun, Tensile behaviors and deformation mechanisms of a nickel-base single crystal superalloy at different temperatures, Mater. Sci. Eng. A. 598 (2014) 154–161.

[70] S. Wei, F. He, C.C. Tasan, Metastability in high-entropy alloys: A review, J. Mater. Res. 33 (2018) 2924–2937.

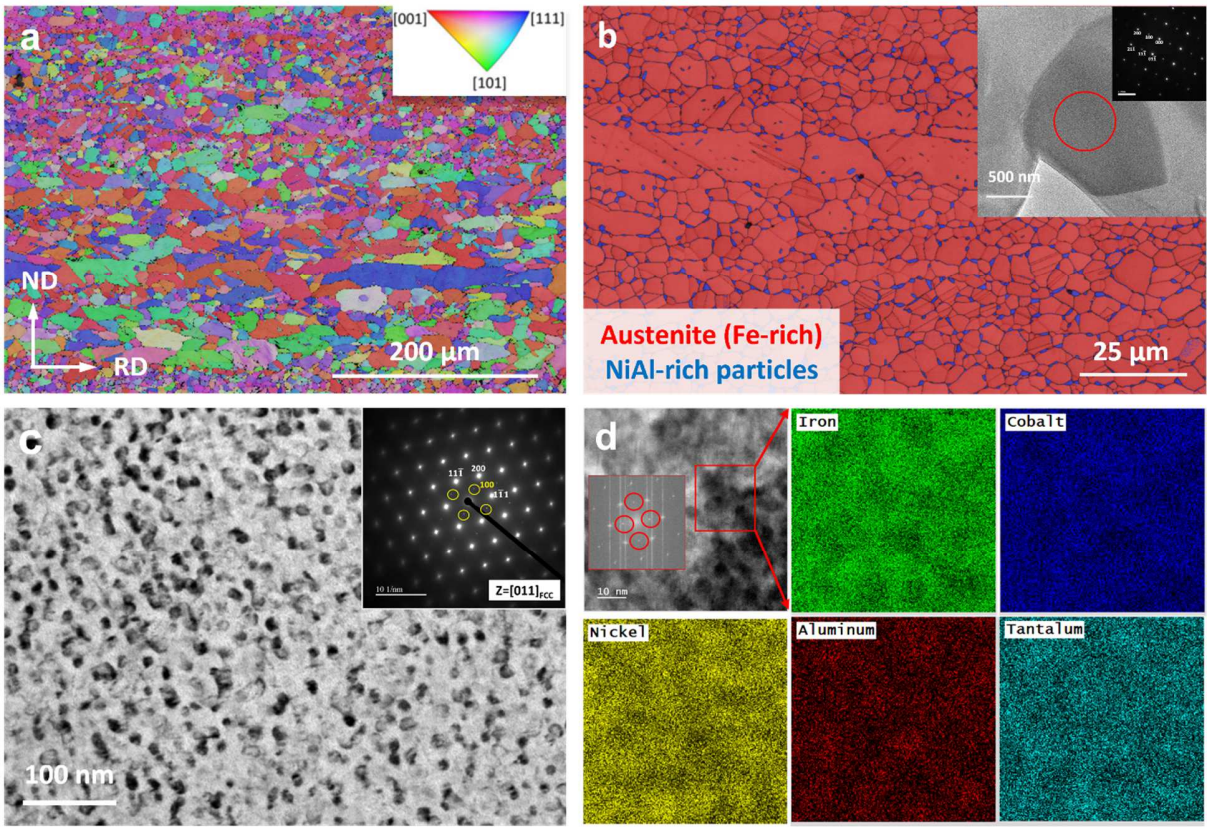

Fig. 1. Microstructure of the Fe-28.2Ni-17Co-11Al-2.5Ta-0.04B (at.%) HEA. (a) EBSD inverse pole figure map showing the heterogeneous structure for FeNiCoAlTaB after annealing and aging. ND - normal direction; RD - rolling direction. (b) EBSD phase map overlaid with band contrast (BC) map of the HEA after annealing at 1200°C for 10 min, showing that NiAl B2-type particles precipitate along grain boundaries. Embedded are the TEM micrograph and the selected area diffraction pattern of the NiAl B2-type particles, zone axis is [011]. (c) TEM micrograph for the aged FeNiCoAlTaB showing the existence of coherent γ′-$L1_2$ precipitates as evidenced by the diffraction pattern. (d) STEM-EDS mapping of the element distribution, confirming that the γ′ particles are mainly composed of Ni, Al, and Ta.

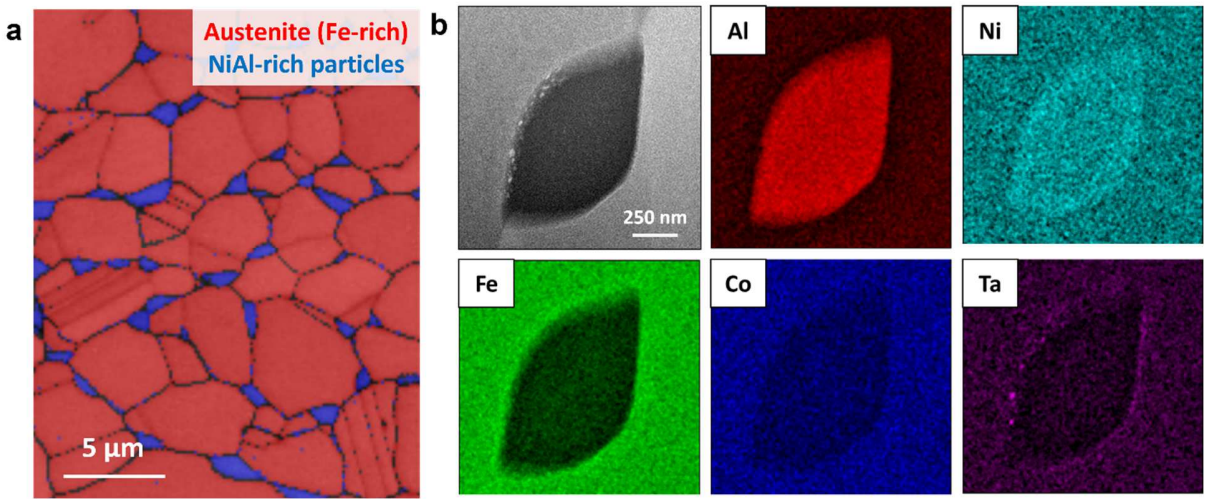

Fig. 2. Distribution and composition of NiAl B2 precipitates after annealing. (a) EBSD phase map for the fine grain areas in the heterostructured FeNiCoAlTaB alloy after annealing at 1400 K for 1 hr, showing the stable heterostructure at high temperature; (b) TEM EDS mapping for the NiAl B2-type precipitates distributed along the grain boundaries, showing the enrichment in Al and Ni in this precipitate.

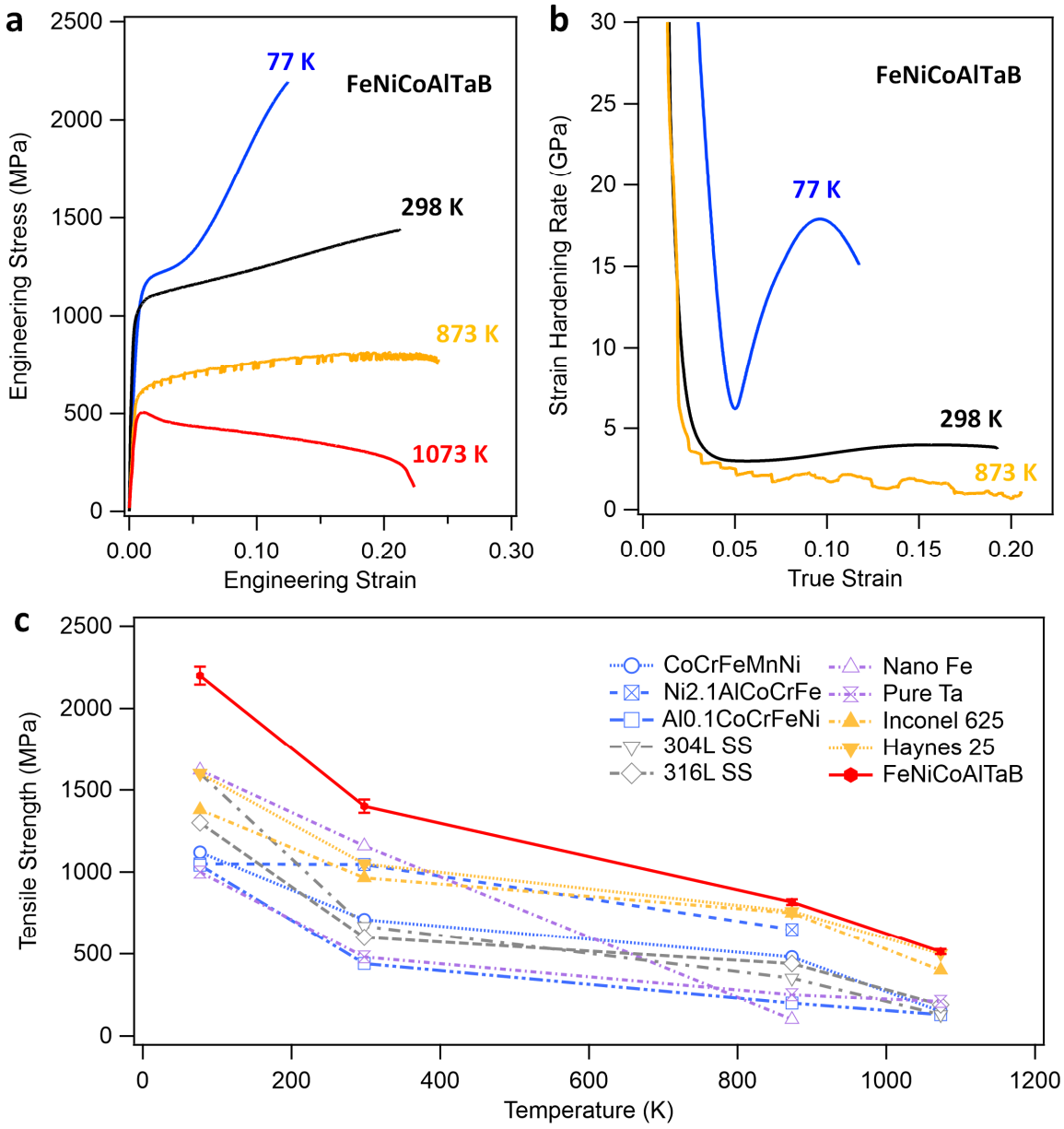

Fig. 3. Mechanical properties of the FeNiCoAlTaB HEA across a wide temperature range from 77 K to 1073 K. (a) Engineering uniaxial tensile stress-strain curves, showing high strength and ductility at 77 K, 298 K, 873 K and 1073 K. (b) Corresponding strain-hardening rates versus true strain at 77K, 298 K and 873 K. (c) Comparison of the tensile strengths as a function of deformation temperature for the FeNiCoAlTaB HEA with those of other high-performance metals and alloys, including HEAs [40-44], stainless steels [22,23], nano-Fe [1], pure Ta [39], and superalloys [23,33,45,46].

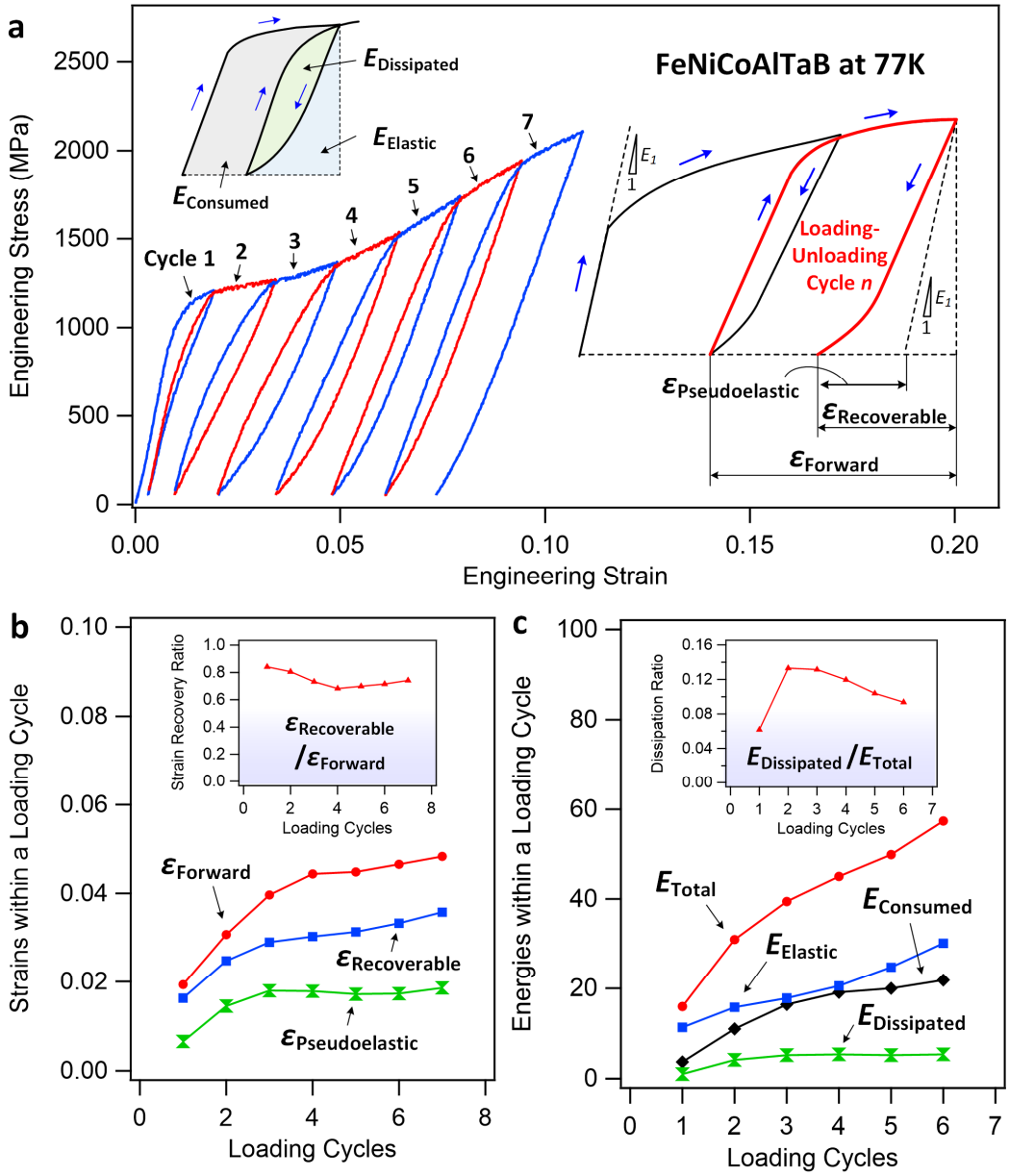

Fig. 4. Pseudoelastic behavior of the FeNiCoAlTaB HEA at a cryogenic temperature of 77 K. (a) Cyclic loading-unloading stress-strain curves at 77 K. The FeNiCoAlTaB alloy exhibits typical pseudoelastic behavior showing large nonlinear recoverable strain upon unloading. (b) Variations in the forward strain ($\varepsilon_{Forward}$), recoverable strain ($\varepsilon_{Recoverable}$), pseudoelastic strain ($\varepsilon_{Pseudoelastic}$), and the strain recovery ratio ($\varepsilon_{Recoverable}/\varepsilon_{Forward}$) with respect to the loading cycles. (c) Variations in the total energy (E_{Total}), elastic energy ($E_{Elastic}$), consumed energy ($E_{Consumed}$), dissipated energy ($E_{Dissipated}$), and the dissipation ratio ($E_{Dissipated}/E_{Total}$) as a function of the number of loading cycles.

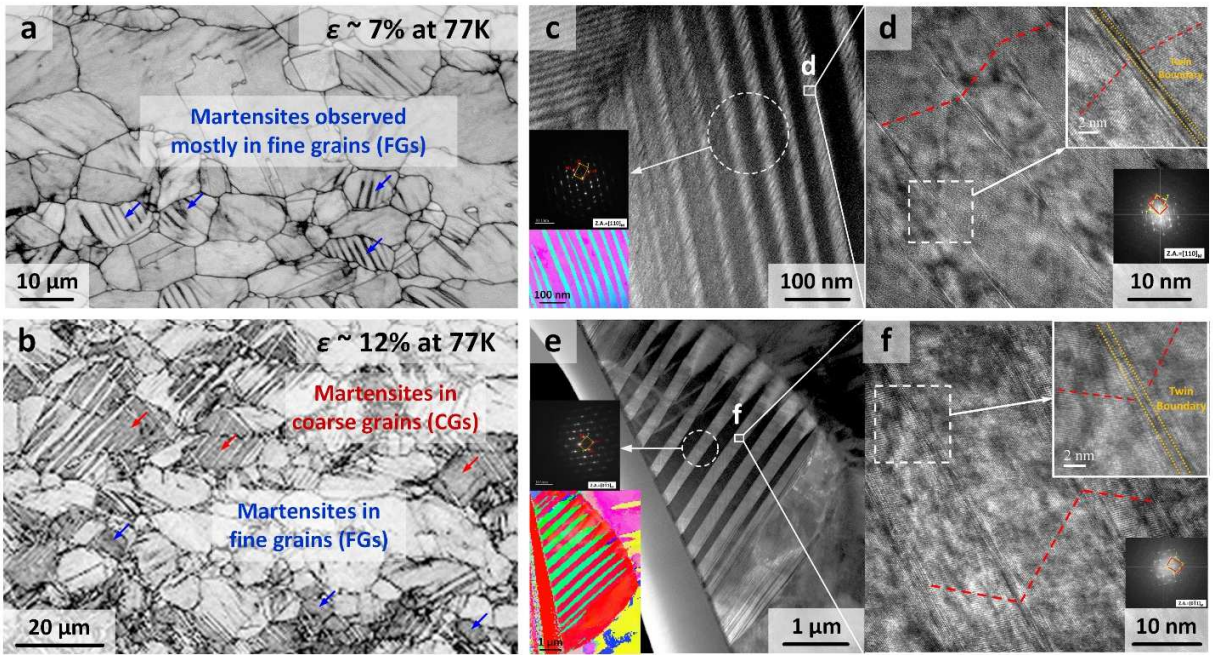

Fig. 5. Microstructure of the FeNiCoAlTaB HEA after tensile testing at 77 K. (a) EBSD band contrast map of the deformed microstructure at a strain of ~7%, showing that the martensite regions are formed mostly in the fine grains. (b) EBSD band contrast map of the deformed microstructure at a strain of ~12%. Martensite regions are fully extended in the fine grains but are also formed in the coarse grains. (c) TEM dark-field image and precession electron diffraction map taken in the coarse grain regions clearly showing the presence of thin-plate martensite. (d) High-resolution TEM image taken inside the martensite phase showing ultrafine nanotwins. (e) TEM dark-field image of the thin-plate martensite and precession electron diffraction map in the fine grains. (f) Nanotwins revealed by high-resolution TEM imaging inside the martensite in the fine grain region.

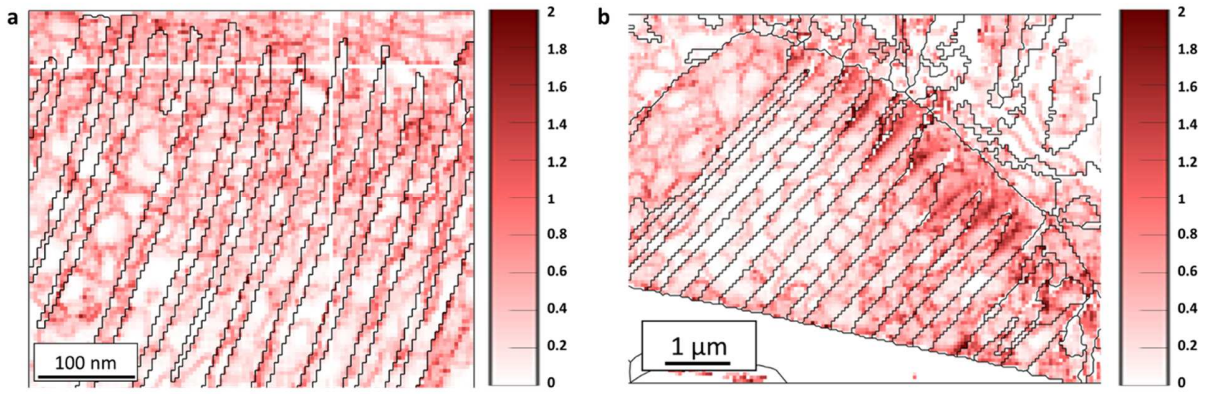

Fig. 6. Local misorientation map of the FeNiCoAlTaB alloy after testing at 77 K. (a) Kernel average misorientation (KAM) map of stress-induced martensite in coarse grains after testing at 77 K; (b) KAM map of the martensite in the corresponding fine grains after testing at 77 K. units: degrees. In this KAM approach, the arithmetic mean of the scalar misorientation between groups of pixels, or kernels, is calculated and mapped. The local misorientation indicates the dislocation activity.

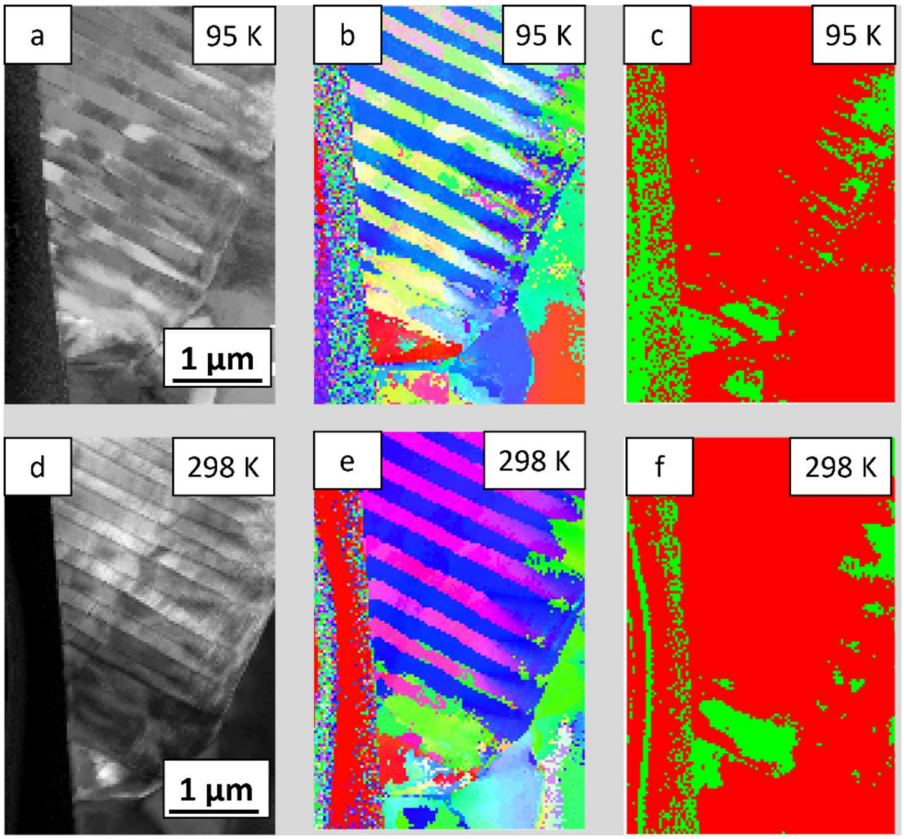

Fig. 7. TEM-PED images for 77K-deformedl FeNiCoAlTaB samples *in situ* characterized at 95 K and 298 K. (a) STEM micrograph, (b) Inverse pole figure, and (c) phase map of the FeNiCoAlTaB sample (after tension test at 77 K) at 95 K, red-martensite, green-austenite. (d) STEM micrograph, (e) Inverse pole figure, and (f) phase map of the same FeNiCoAlTaB sample heated up to 298 K. No obvious phase transformation was observed during the heating process.

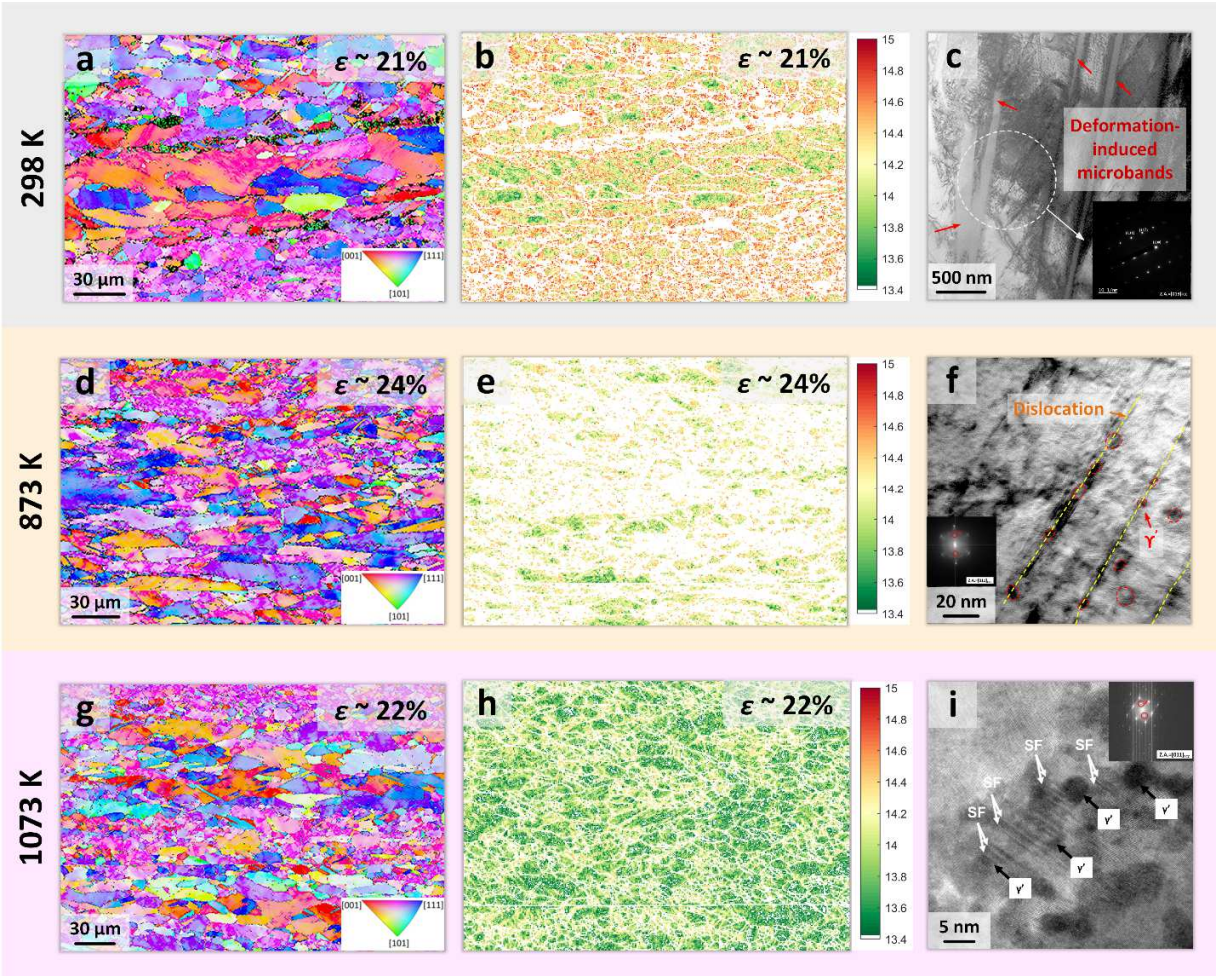

Fig. 8. Microstructure of the FeNiCoAlTaB HEA after tensile testing at elevated temperatures. (a) EBSD inverse pole figure map after testing the alloy at 298 K; (b) Geometrically-necessary dislocation density map corresponding to Fig. 8a, units: $\log_{10}(m^{-2})$; (c) TEM bright-field micrograph of the microbands formed after deformation at ambient temperature; (d) EBSD inverse pole figure after testing the alloy at 873 K; (e) Geometrically-necessary dislocation density map corresponding to Fig. 8d, units: $\log_{10}(m^{-2})$; (f) TEM bright-field micrograph of FeNiCoAlTaB after testing at 873 K, showing the interaction between precipitates and dislocations; (g) EBSD inverse pole figure after testing the alloy at 1073 K, showing that the heterostructure still remains; (h) Geometrically-necessary dislocation density map corresponding to Fig. 8g, units: $\log_{10}(m^{-2})$; (i) HRTEM bright-field micrograph of stacking faults in the deformed FeNiCoAlTaB alloy after testing at 1073 K.

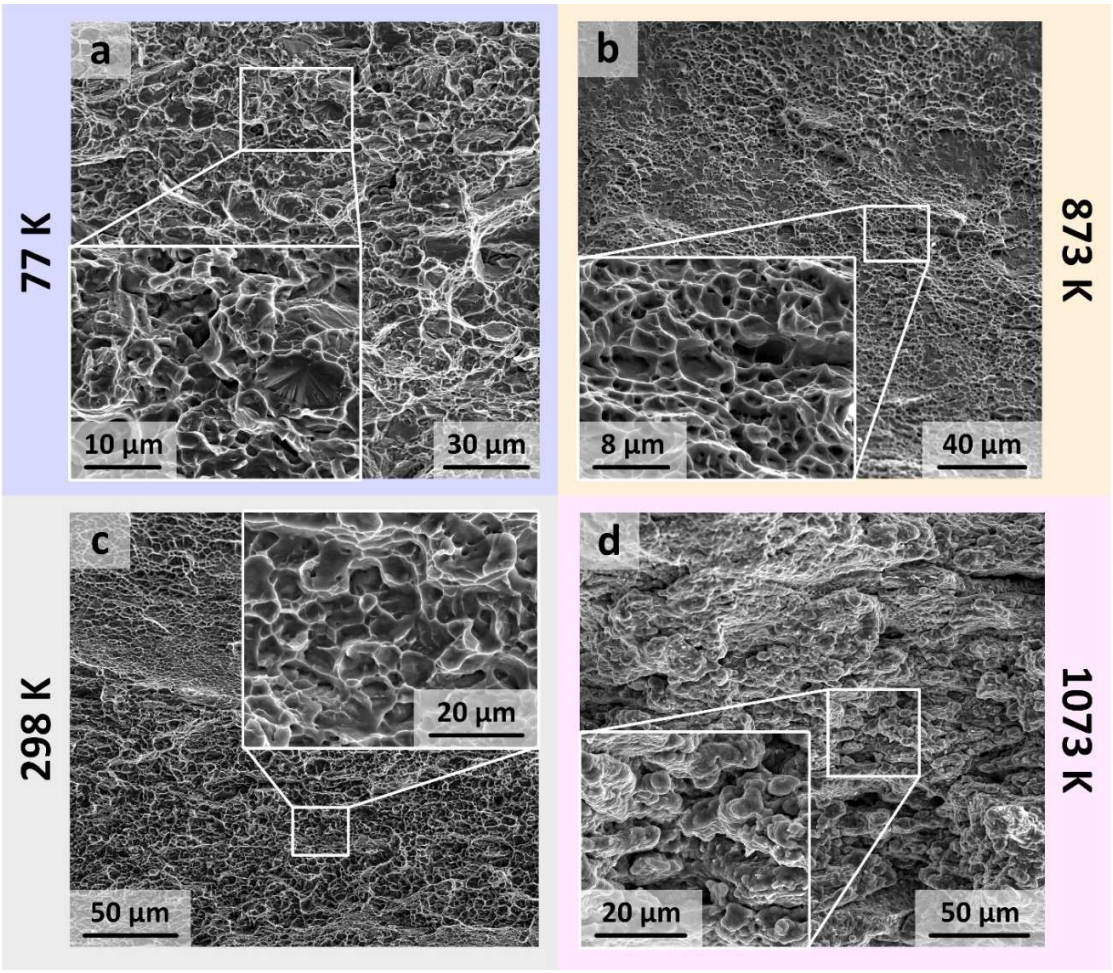

Fig. 9. Fracture surface analysis of the FeNiCoAlTaB HEA after testing at cryo-to-elevated temperatures. SEM micrographs of the fracture surfaces after tensile testing at (a) 77 K, (b) 298 K, (c) 873 K, and (d) 1073 K, showing a ductile failure mechanism of microvoid coalescence.

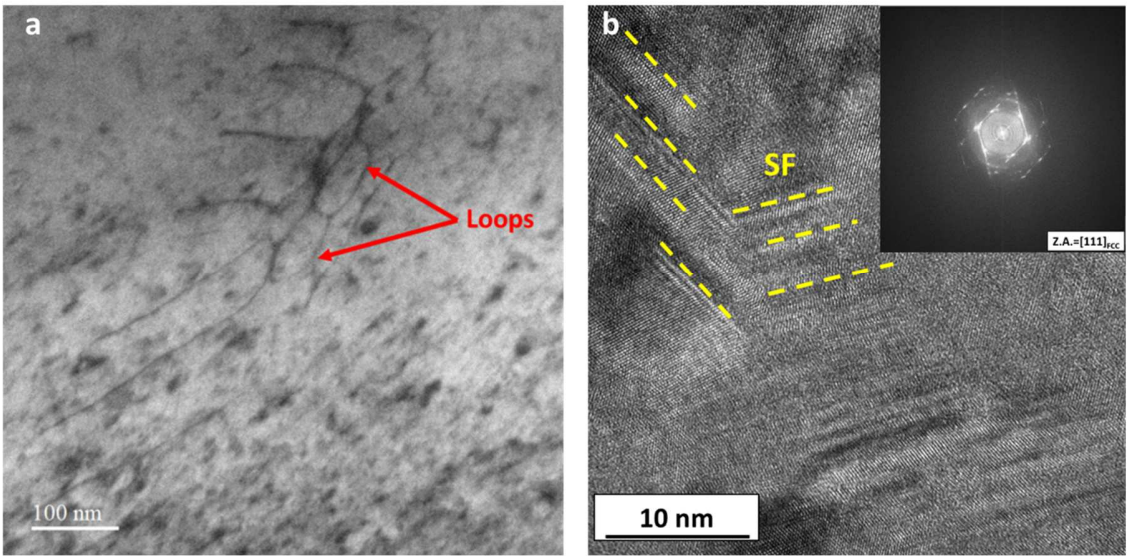

Fig. 10. Dislocation activity at elevated temperature. TEM micrograph of (a) dislocation loops and (b) stacking faults in the deformed FeNiCoAlTaB alloy after testing at 1073K.

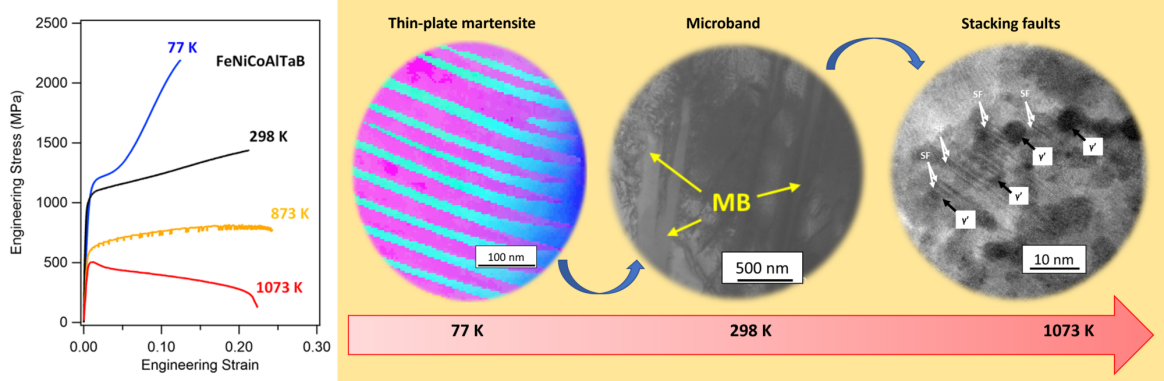
2500
2000
1500
1000
500
0
Engineering Stress (MPa)
0.00
0.10
0.20
0.30
Engineering Strain
77 K
FeNiCoAlTaB
298 K
873 K
1073 K
Thin-plate martensite
100 nm
Microband
MB
500 nm
Stacking faults
SF
SF
SF
γ'
γ'
γ'
γ'
10 nm
77 K
298 K
1073 K